PNAS RESEARCH ARTICLE | CHEMISTRY

Stabilizing $Ti_3C_2T_x$ MXene flakes in air by removing confined water

Hui Fang[a], Anupma Thakur[b,c], Amirhossein Zahmatkeshsaredorahi[d], Zhenyao Fang[a], Vahid Rad[e], Ahmad A. Shamsabadi[a], Claudia Pereyra[a], Masoud Soroush[e], Andrew M. Rappe[a], Xiaoji G. Xu[d], Babak Anasori[b,c,f,1], and Zahra Fakhraai[a,1]

Affiliations are included on p. 8.

Edited by Elisa Riedo, New York University, New York, NY; received January 2, 2024; accepted June 1, 2024 by Editorial Board Member Pablo G. Debenedetti

MXenes have demonstrated potential for various applications owing to their tunable surface chemistry and metallic conductivity. However, high temperatures can accelerate MXene film oxidation in air. Understanding the mechanisms of MXene oxidation at elevated temperatures, which is still limited, is critical in improving their thermal stability for high-temperature applications. Here, we demonstrate that $Ti_3C_2T_x$ MXene monoflakes have exceptional thermal stability at temperatures up to 600 °C in air, while multiflakes readily oxidize in air at 300 °C. Density functional theory calculations indicate that confined water between $Ti_3C_2T_x$ flakes has higher removal energy than surface water and can thus persist to higher temperatures, leading to oxidation. We demonstrate that the amount of confined water correlates with the degree of oxidation in stacked flakes. Confined water can be fully removed by vacuum annealing $Ti_3C_2T_x$ films at 600 °C, resulting in substantial stability improvement in multiflake films (can withstand 600 °C in air). These findings provide fundamental insights into the kinetics of confined water and its role in $Ti_3C_2T_x$ oxidation. This work enables the use of stable monoflake MXenes in high-temperature applications and provides guidelines for proper vacuum annealing of multiflake films to enhance their stability.

MXene | thermal stability | stable monoflake | confined water | MXene oxidation

Significance

Different mechanisms have been proposed for MXene oxidation. However, the specific oxidation process in dry films remains a topic of ongoing debate. Here, we demonstrate that confined water, trapped between stacked flakes, causes $Ti_3C_2T_x$ MXene oxidation in ambient. As such, $Ti_3C_2T_x$ monoflakes have intrinsically high thermal stability and can withstand temperatures as high as 600 °C , well beyond the typical 300 °C oxidation temperature of multiflakes. Moreover, confined water is extremely stable and can be removed after vacuum annealing at 600 °C. This study modifies the main chemical pathway for $Ti_3C_2T_x$ oxidation, details the critical role of water in 2D material degradation, and provides a blueprint for producing extremely stable MXenes for various applications.

Two-dimensional (2D) transition-metal carbides, nitrides, or carbonitrides (MXenes) have made pronounced impacts in various application fields such as energy storage, (1, 2) optoelectronics, (3) electromagnetic interference shielding, (4) wearable electronics, (5) water purification, (6) and biomedicine, (7). These applications are enabled by MXenes' exceptional electronic, mechanical, electrochemical, and optical properties. (8–10) MXenes have the general chemical formula of $M_{n+1}X_nT_x$ ($n = 1$ to 4), where $(n + 1)$ atomic layers of an early transition metal (M) from groups three to six are interleaved by n atomic layers of carbon and/or nitrogen (X), and the outermost exposed M layers are terminated with a combination of surface groups (T = −F, −O, −OH) (10, 11). It has been reported that $Ti_3C_2T_x$ MXene films are environmentally stable for many years when stored in air at room temperature. (12) However, these MXene films can readily oxidize upon heating in air, due to humidity given their metastable surface terminations (13, 14). This degradation process limits their high-temperature applications.

The oxidation mechanism of MXenes, especially for $Ti_3C_2T_x$, has been extensively investigated (14–16). Generally, $Ti_3C_2T_x$ films can react with oxygen and water to generate TiO_2 and amorphous carbon sheets in air (13, 14, 17). MXene oxidation can be expedited in aqueous solutions, as water can trigger a hydrolysis reaction, which can become the primary pathway to degradation (15, 18). MXene degradation rate is further accelerated at elevated temperatures (19). For instance, for a colloidal solution of delaminated $Ti_3C_2T_x$ flakes to be fully oxidized, the degradation time is reduced from several days at room temperature(18) to several hours when the sample is held at 400 °C in the air (20). It has been shown that MXene oxidation can be affected by intercalated H_2O and surface terminations (17), which can be controlled by posttreatment annealing in vacuum at elevated temperatures (16, 21). For instance, the desorption of intercalated H_2O has been reported to occur below 200 °C (16, 22, 23), followed by the removal of −OH termination groups, which occur in the temperature window of 200 °C to 400 °C (21). A further temperature increase results in the removal of the −F and −O groups (14). As the presence of water has been considered to be the main reason for oxidation, 200 °C vacuum annealing has been widely adopted in the literature as an approach to improving the stability of $Ti_3C_2T_x$ MXene (24, 25), with moderate success. Moreover, it

Author contributions: H.F., B.A.,and Z. Fakhraai designed research; H.F., A.T., A.Z., Z. Fang, V.R., and C.P. performed research; H.F., Z. Fang, and V.R. analyzed data; and H.F., A.T., A.Z., Z. Fang, V.R., A.A.S., C.P., M.S., A.M.R., X.G.X., B.A., and Z. Fakhraai wrote the paper.

The authors declare no competing interest.

This article is a PNAS Direct Submission. E.R. is a guest editor invited by the Editorial Board.

[1]To whom correspondence may be addressed. Email: banasori@purdue.edu or fakhraai@sas.upenn.edu.

This article contains supporting information online at https://www.pnas.org/lookup/suppl/doi:10.1073/pnas.2400084121/-/DCSupplemental.

Published July 5, 2024.

has been reported that $Ti_3C_2T_x$ MXene film stability in harsh environments (100% relative humidity, 70 °C) can be improved after hydrogen annealing at 900 °C (26).

Most investigations of $Ti_3C_2T_x$ oxidation have been performed on MXene multiflake films or colloidal solutions (14, 20). As such, the details of the oxidation process at the single- or few-flake level are lacking. Due to their high surface-to-volume ratios, $Ti_3C_2T_x$ MXene monoflakes have unique properties, such as higher conductivity (27), friction force (28), and Young's modulus (29). While it has previously been reported that single-layer MXene films have high stability at room temperature (30), it is also important to understand and improve the thermal stability of monoflakes at elevated temperatures, to broaden their use in high-temperature applications.

In this work, we investigate the detailed role of confined water in the thermal stability of $Ti_3C_2T_x$ MXene in monoflakes and multiflakes films, using various spectroscopy and atomic force microscopy (AFM) techniques and density functional theory (DFT) calculations. We find that $Ti_3C_2T_x$ monoflakes are exceptionally stable against oxidation and retain their conductivity and other properties at temperatures as high as 600 °C in air. In contrast, stacked flakes readily oxidize in air upon heating to 300 °C to form TiO_2 nanoparticles, which are more prevalent when a higher number of flakes are stacked. We conclusively report that confined interflake water, as opposed to ambient humidity, causes multiflake oxidation. We demonstrate that this confined water can only be fully removed under vacuum by annealing to 600 °C, a much higher annealing temperature than previously employed. Upon the removal of confined water in $Ti_3C_2T_x$ films, the thermal stability of stacked flakes is dramatically increased, allowing them to withstand heating to 600 °C in air, without oxidation. These findings fill the gap that existed in understanding the variations in observed levels of oxidation in monoflakes, stacked flakes, and bulk $Ti_3C_2T_x$, suggest a change in standard annealing conditions of MXenes for stabilizing multiflake films, and enable MXene applications at extremely high temperatures.

Results and Discussions

$Ti_3C_2T_x$ MXene was synthesized by selectively etching the optimized Ti_3AlC_2 MAX phase (31) followed by delamination at 65 °C under argon (details in *Materials and Methods*). The MAX are layered, hexagonal carbides and nitrides, with the general formula $M_{n+1}AX_n$, where M is an early transition metal, A is an A-group (13 or 14 groups) element and X is either carbon and/or nitrogen. Thin films with different numbers of stacked flakes of $Ti_3C_2T_x$ were fabricated on Si substrates via spin-coating from aqueous solutions (details in *Materials and Methods*). The thermal stability of MXene films was measured through the temperature dependence of optical resistivity via in situ spectroscopic ellipsometry (SE) (23). Fig. 1*A* shows an example of resistivity as a function of temperature, upon thermal cycling to various temperatures at a rate of 10 °C/min in ambient conditions, for an As-prepared $Ti_3C_2T_x$ film. The resistivity of this film ($0.45 \pm 0.03 \times 10^{-3}$ Ω·cm at room temperature) was deduced based on a fitted Drude Oscillator to the near infrared (IR) spectral region(23), which demonstrates metallic conductivity. More details of SE fitting procedures and results can be found in *SI Appendix*, Note S1 and Fig. S1 and Table S1.

Determining the Oxidation Onset Temperature and Products. Upon heating under air from room temperature to 200 °C (Fig. 1*A*, gray curve), the film resistivity increases with temperature, consistent with the metallic nature of $Ti_3C_2T_x$. The resistivity recovers its original value when the sample is cooled back to room temperature, meaning that the film is thermally stable within this temperature window. However, when the temperature is increased to 300 °C (Fig. 1*A*, pink curve) in air, a sudden jump in resistivity is observed from (0.49 ± 0.02) $\times 10^{-3}$ to (0.72 ± 0.11) $\times 10^{-3}$ Ω·cm after a 3-min hold at this temperature, which is irreversible upon cooling. This trend continues upon heating to 400 °C followed by another 3-min hold (Fig. 1*A*, blue curve), increasing the resistivity to above (1.21 ± 0.31) $\times 10^{-3}$ Ω·cm. These results are the averaged values from 5 independent measurements on different samples. The irreversible change in resistivity can be attributed to decreasing free electron density upon $Ti_3C_2T_x$ oxidation and the formation of semiconducting TiO_2 (15, 23, 27). This onset of

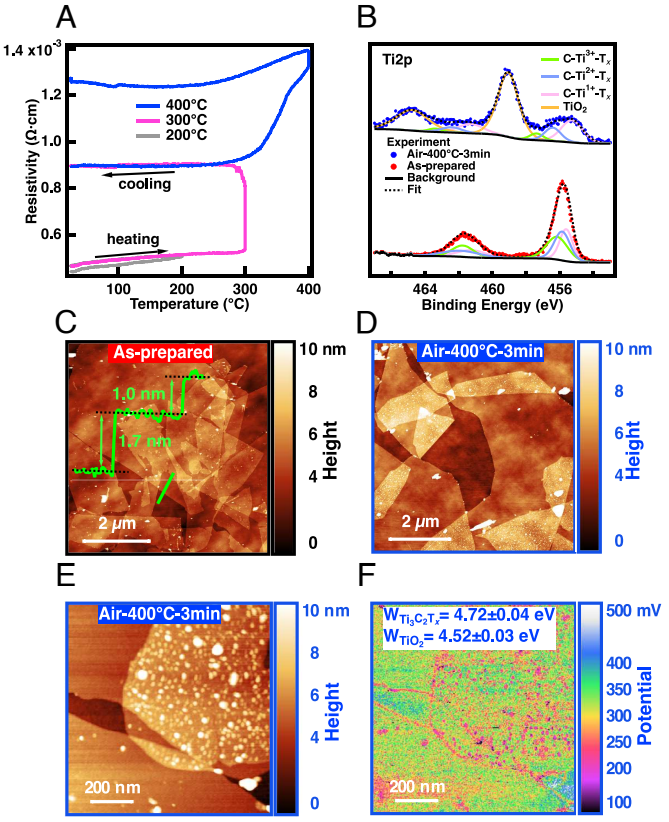

Fig. 1. Stacked $Ti_3C_2T_x$ flakes are readily oxidized, while monoflakes are thermally stable. (*A*) Resistivity vs. temperature of an As-prepared $Ti_3C_2T_x$ film (1.5 nm thickness) spun-cast on a Si substrate, measured with in situ SE upon three consecutive thermal cycling in air (humidity 10 to 20%) at 10 °C/min to 200 °C (gray curve), 300 °C (pink curve), and 400 °C (blue curve), with a 3 min hold time at each temperature. Arrows show the direction of heating and cooling. The oxidation onset, where an irreversible increase in resistivity occurs, is measured at 300 °C. (*B*) Ti 2p XPS spectra of an As-prepared $Ti_3C_2T_x$ film before (*Bottom*) and after air annealing treatment at 400 °C for 3 min (*Top*). The details of fitting for each peak can be found in *SI Appendix*, Note S2 and Tables S2 and S4. (*C*) AFM image of an As-prepared $Ti_3C_2T_x$ film on a Si substrate. The *Inset* shows the height profile along the green line. (*D*) AFM image of a similarly prepared film as in (*C*) upon annealing in air at 400 °C for 3 min (denoted as Air-400 °C-3 min). White dots, which appear only on stacked flakes, indicate the formation of TiO_2 nanoparticles upon oxidation. Small-area AFM topography (*E*) and corresponding surface potential (*F*) images of an air-annealed (Air-400 °C-3 min) film show monoflake and biflake $Ti_3C_2T_x$ regions on Si substrate. Surface potential (*F*) is reduced on oxidized regions, which correspond to the white nanoparticles in (*E*) as well as the flake edges. The black and blue image borders in (*C*–*F*) denote As-prepared and Air-400 °C-3 min films, respectively.

irreversible oxidation at 300 °C is more apparent when resistivity is measured upon cycling to successively higher temperatures as shown in *SI Appendix*, Fig. S1C and at a higher cycling rate as shown in *SI Appendix*, Fig. S2. The amplitude of the signature near-IR $Ti_3C_2T_x$ extinction peak also decreases upon heating to above 300 °C (*SI Appendix*, Fig. S1D), further corroborating the onset of $Ti_3C_2T_x$ degradation at 300 °C. X-ray photoelectron spectroscopy (XPS) measurements show the formation of TiO_2 as the primary oxidation reaction product. XPS was performed on samples before and after annealing in air to 300 °C and 400 °C, respectively, with a 3-min hold at each temperature. The detailed fitting procedure for the XPS spectra can be found in the literature (32) and in *SI Appendix*, Note S2. The fitted results are tabulated in *SI Appendix*, Tables S2–S4. The most prevalent signals in the Ti 2p spectra (Fig. 1*B*) correspond to the C−Ti−T_x bonding (dominant before annealing) and TiO_2 (dominant after air annealing at 400 °C). As the air annealing temperature is increased, complementary TiO_2 signals increase, as also observed in the O 1s spectra (*SI Appendix*, Fig. S3). Combined with the results shown in Fig. 1*B* and *SI Appendix*, Fig. S3*A*, the data suggest that the percentage of TiO_2 increases with increasing annealing temperature. These results are consistent with the previously reported results for both As-prepared and oxidized $Ti_3C_2T_x$ (32, 33). With air annealing temperature increasing, the C–C signal also increases in the C 1s spectra (*SI Appendix*, Fig. S3*C*) due to the formation of carbon, as one of the oxidation products (13, 34). This is also consistent with the previous C 1s XPS results for oxidized $Ti_3C_2T_x$ (33, 35).

MXene Monoflake is Stable Toward Oxidation in Air. To gain insight into the morphological changes of $Ti_3C_2T_x$ upon oxidation, the morphology of $Ti_3C_2T_x$ thin films before and after air annealing (held at 400 °C for 3 min) were characterized using AFM. The results are shown in Fig. 1 *C*–*E*. As seen in Fig. 1*C*, As-prepared films (before oxidation, black border) mostly consist of randomly stacked $Ti_3C_2T_x$ flakes. As shown by the example height profile (green line) in Fig. 1*C*, the flake heights relative to each other are measured to be 1.02 ± 0.04 nm, which is consistent with the previously reported thickness of $Ti_3C_2T_x$ single flakes (27, 36). However, $Ti_3C_2T_x$ monoflakes as well as the first flakes in a stack, as counted from the substrate (*SI Appendix*, Fig. S4), typically show higher heights of 1.71 ± 0.04 nm. *SI Appendix*, Fig. S4 and Note S3 schematically show these height values and definitions of flake numbers in a stacked biflake. Previous measurements on $Nb_4C_3T_x$ MXenes also reported a higher thickness for the first flake on the substrate compared to other flakes (37). Upon oxidation (Fig. 1 *D* and *E*, blue border), the stacked regions show increased roughness with numerous randomly sized nanoparticles on their surfaces, indicating the formation of TiO_2. Notably, monoflakes do not appear to show any change in their morphology and height and remain stable despite the overall thermal degradation of the film after annealing to 400 °C in air, as measured through SE and XPS (Fig. 1 *A* and *B*).

To determine the extent of monoflake stability, the effects of air annealing time and temperature were also investigated. After prolonging the air annealing time from 3 min to 2 h at 400 °C, there was still no TiO_2 formation on monoflake surfaces (*SI Appendix*, Fig. S5*A*). Increasing the oxidation temperature to 600 °C with a 3-min hold also did not result in any TiO_2 formation on monoflakes either (*SI Appendix*, Fig. S5*B*). However, the monoflakes eventually oxidized after holding MXene thin films for 2 h at 600 °C in air, which was confirmed by the appearance of the TiO_2 nanoparticles on monoflake surfaces (*SI Appendix*, Fig. S5*C*). As such, it is clear that the $Ti_3C_2T_x$ monoflakes can withstand temperatures as high as 400 °C for a prolonged duration of time (at least for 2 h) and temperatures as high as 600 °C for a brief period of time without bulk oxidation. These findings provide a valuable opportunity to use $Ti_3C_2T_x$ monoflakes for high-temperature applications. It would be valuable to explore the extent of this durability upon long-term storage, which will be detailed in our upcoming work.

To further confirm that the chemical structure of monoflakes is unperturbed and determine the chemical composition of the nanoparticles on stacked flake surfaces, kelvin probe force microscopy (KPFM) was employed to determine the surface work function. AFM topography and corresponding surface potential images of an oxidized film (annealed in Air-400 °C-3 min) with monoflakes and biflakes are shown in Fig. 1 *E* and *F*. Consistent with the height difference in Fig. 1*E*, the surface potential of nanoparticles (pink colored regions in Fig. 1*F*) are quite different than the unoxidized regions of the biflake as well as the monoflake surfaces (seen as green color in the background of Fig. 1*F* and in *SI Appendix*, Fig. S6). Based on these data, the work function of the flat regions is estimated to be 4.72 ± 0.04 eV, which is in agreement with the previously reported values for $Ti_3C_2T_x$ (38). The work function for the nanoparticles is measured to be 4.52 ± 0.03 eV, which is also consistent with the reported values for TiO_2 (39), further confirming that the nanoparticles are primarily made of TiO_2. Interestingly, despite the lack of significant height increase at the MXene edges (Fig. 1*E*), the surface potential of the edges for both monoflakes and biflakes are similar to these of the TiO_2 nanoparticles, as seen in Fig. 1*F*. This implies that $Ti_3C_2T_x$ edges are overall more prone to oxidation, even in otherwise stable monoflakes. This is likely due to the dangling bonds and increased number of defects on the edges, as has been previously predicted (27).

The stability of $Ti_3C_2T_x$ monoflakes and the rapid oxidation of stacked flakes are observed regardless of the supporting substrate and synthesis method. Similar oxidation features were observed for $Ti_3C_2T_x$ films on mica substrate (*SI Appendix*, Fig. S7) and stoichiometric $Ti_3C_2T_x$, synthesized from the oxycarbide Ti_3AlC_2 MAX phase (40) (*SI Appendix*, Fig. S8). More details can be found in *SI Appendix*, Note S4.

The Effect of Vacuum Annealing Strategies on Stacked-Flake Stability. Vacuum annealing at 200 °C has been widely adopted as an approach to improve $Ti_3C_2T_x$ stability by removing water (24, 25). To investigate the effect of vacuum annealing on the stability and morphology of stacked flakes, vacuum annealing was performed on $Ti_3C_2T_x$ films at various temperatures as schematically shown in Fig. 2 (*Top* row, marked with green shadow). The vacuum-annealed samples were then subjected to the same air annealing oxidation test as the As-prepared samples (schematically shown at the *Bottom* row of Fig. 2, blue box). For simplicity, Vacuum-annealed samples are denoted as Vacuum-*T*-*t*, where T and t are the annealing temperature and time, respectively. AFM images of As-prepared, Vacuum-200 °C-24 h, Vacuum-500 °C-5 h, and Vacuum-600 °C-2 h films are shown in *SI Appendix*, Fig. S9 *A*–*D*. There is no evidence of TiO_2 nanoparticles on the surfaces of either monoflakes and stacked flakes in these images, indicating that vacuum annealing even at 600 °C for 2 h does not result in $Ti_3C_2T_x$ degradation. XPS results in *SI Appendix*, Fig. S10 also do not show any evidence of TiO_2 formation upon vacuum annealing. This is in line with the previous results indicating the stable structure of 2D

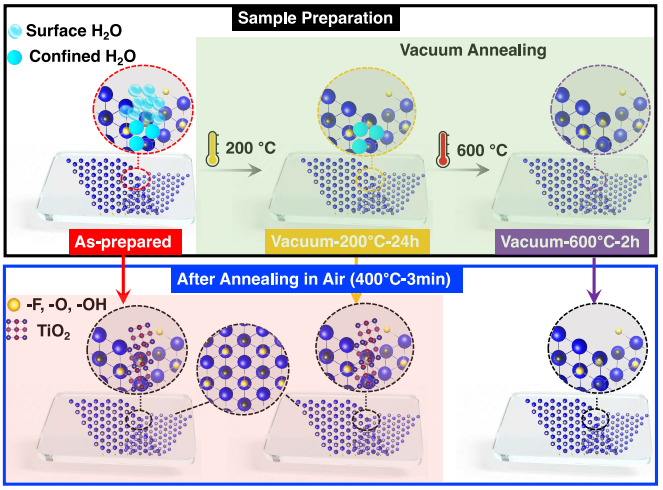

Fig. 2. Schematic description of the experimental steps. The *Top* row (black box) shows sample preparation steps. From *Left* to *Right*; As-prepared (pristine) $Ti_3C_2T_x$ sample (red label) has surface and confined water trapped in the interflake region, vacuum annealing (marked by green shadow) at 200 °C for 24 h (orange label) removes the surface adsorbed water, and vacuum annealing at 600 °C for 2 h (purple label) further removes the confined water. The *Bottom* row (blue box) shows the structure of the same samples after air annealing, typically at 400 °C for 3 min, respectively. In samples originally containing surface adsorbed and confined water (marked by pink shadow), TiO_2 is only detected but only in the stacked-flake regions, while the monoflakes are stable. In the sample annealed in vacuum at 600 °C for 2 h, in which both surface adsorbed and confined water are removed, no evidence of oxidation is observed anywhere.

$Ti_3C_2T_x$ after heating to 600 °C in vacuum, confirmed by the scanning electron microscope and X-ray diffraction (19). The effects of vacuum annealing rate and holding time at various temperatures were examined. No differences between 60 °C/min and 10 °C/min heating rates and no oxidation after vacuum annealing to 600 °C were observed (*SI Appendix*, Fig. S11). The effect of holding time at 600 °C for 1 h, 2 h, and 5 h was also tested. It was found that 1 h is not enough to protect $Ti_3C_2T_x$ from oxidation (*SI Appendix*, Fig. S12).

Fig. 3 *A* and *B* depict the AFM morphology of Vacuum-200 °C-24 h and Vacuum-600 °C-2 h $Ti_3C_2T_x$ films after air annealing at 400 °C for 3 min, respectively. The corresponding AFM images under other vacuum annealing conditions are shown in *SI Appendix*, Fig. S13. Not surprisingly, the monoflakes of all of the Vacuum-annealed samples are very stable and do not show any significant change in their flat morphology. However, when the vacuum annealing temperature was below 500 °C, stacked flakes of $Ti_3C_2T_x$ oxidized upon subsequent annealing in air (Fig. 3*A* and *SI Appendix*, Fig. S13 *A–C*). Interestingly, increased stacking contributes to faster rate of oxidation in partially Vacuum-annealed films. For example *SI Appendix*, Fig. S13*C* and the corresponding deduced values in *SI Appendix*, Fig. S14, show that triflakes have an even higher roughness with larger TiO_2 nanoparticles on their surfaces than biflakes. In other words, the thicker the deposited $Ti_3C_2T_x$ film, the easier it is to oxidize. These observations imply that some water is present in stacked flakes despite high-temperature annealing in vacuum, as schematically shown in Fig. 2. In contrast, in the samples that were vacuum annealed at 600 °C for 2 h, $Ti_3C_2T_x$ biflakes, and other stacked flakes did not show any sign of oxidation, as nanoparticles were not observed on their surfaces.

High-Temperature Vacuum Annealing Dramatically Improves Stacked-Flake Stability. The dramatic improvement of the air stability of Vacuum-600 °C-2 h films as observed by the absence of TiO_2 nanoparticles after air annealing at 400 °C, is more clearly evident in AFM images of biflakes (Fig. 3*B* and *SI Appendix*, Fig. S15). Increasing the oxidation temperature to 600 °C with a 3-min hold still did not result in the biflakes oxidation in air (similar to the AFM image in Fig. 3*B*, not shown here). The distribution of height values is also quantitatively different in biflakes of Vacuum-600 °C-2 h films than those of Vacuum-200 °C-24 h films as seen in their corresponding AFM height histograms. The height histogram of a Vacuum-600 °C-2 h biflake (Fig. 3*D*) can be fitted well by a Gaussian function, representing a flat morphology with random surface roughness. (41) However, there is an asymmetric tail at higher height values of the corresponding Gaussian peak in a biflake of the Vacuum-200 °C-24 h film (Fig. 3*C*). This asymmetric distribution can be fitted well with a lognormal function (*Inset* of Fig. 3*C*), which is analogous to distributions observed in nucleation and growth of other types of nanoparticles (42). As such, the observed distribution, with a larger number of smaller nanoparticles, can be attributed to the formation and growth of TiO_2 nanoparticles on the biflake surface upon air annealing. More details of the fitting protocols are provided in *SI Appendix*, Note S5. The peak value of the lognormal distribution, 0.56 ± 0.01 nm, represents the estimated TiO_2 nanoparticle height. Similarly, for both samples, the maximum of the Gaussian distribution can be attributed to the thickness. The root mean square roughness (RMS) of a biflake was directly measured from the AFM images (square marked areas in Fig. 3 *A* and *B*) during data processing, representing the surface roughness of the areas.

Fig. 3*E* compares the measured RMS values of monoflakes and biflakes with the average height of TiO_2 nanoparticles at different vacuum annealing temperatures. Each point has its SD, averaged from three different AFM measurements on different MXene films. In oxidized biflakes (annealed below 500 °C), the RMS roughness and TiO_2 height are similar (gray and orange curves), and decrease with increasing annealing temperature. In contrast, in the unoxidized 600 °C-2 h film, where TiO_2 nanoparticles are not observed, the RMS roughness of the biflake is the same as that of monoflake, indicating that the single flake properties are conserved in these films. Vacuum annealing at 600 °C for 2 h appears to completely suppress oxidation even in stacked flakes. The RMS values of monoflakes remain constant regardless of annealing conditions, further confirming the impressive stability of $Ti_3C_2T_x$ MXene monoflakes. In situ SE experiments also demonstrate the exceptional thermal stability of the Vacuum-600 °C-2 h film against oxidation upon air annealing(Fig. 3*F*). Unlike the As-prepared sample that readily oxidizes upon thermal cycling to above 300 °C (Fig. 1*A*), the room-temperature resistivity of the Vacuum-600 °C-2 h film remains unchanged after three thermal cycles up to 400 °C.

Confined Water Is the Main Reason for MXene Oxidation. Intuitively, a monoflake is expected to be more susceptible to oxidation, because it has a higher surface-to-volume ratio than a biflake, resulting in a higher exposure of its atoms to the ambient humidity and oxygen. However, the exact opposite is seen here for both As-prepared (Fig. 1) and moderately Vacuum-annealed $Ti_3C_2T_x$ films (Fig. 3*A*), where monoflakes are observed to be exceptionally stable toward oxidation even after prolonged annealing at high temperatures in air (*SI Appendix*, Fig. S5), and biflakes are observed to degrade readily unless vacuum annealing is performed at 600 °C for 2 h. To understand this

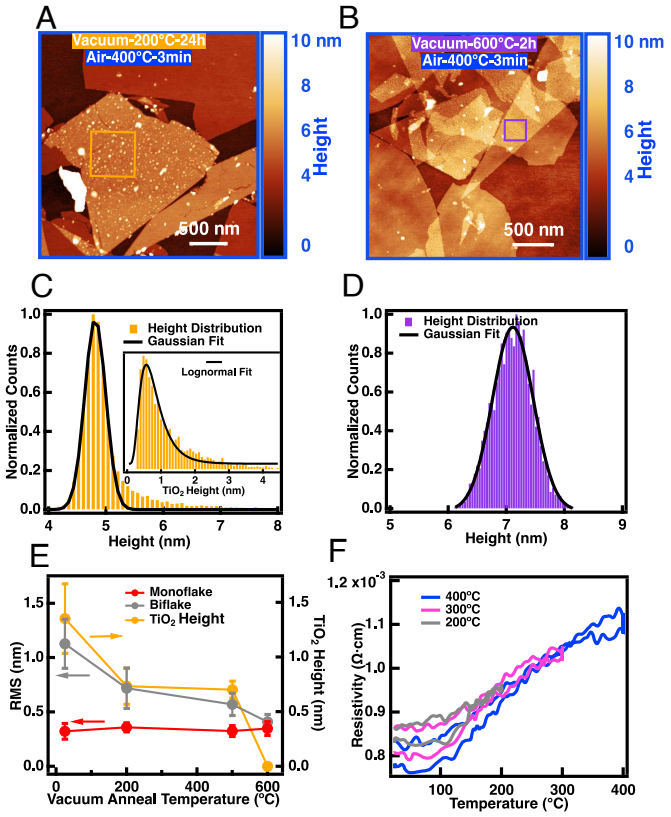

Fig. 3. Effect of vacuum annealing temperature on stacked flake oxidation. (*A* and *B*) The AFM topography images of the Vacuum-200 °C-24 h and 600 °C-2 h $Ti_3C_2T_x$ films on Si substrate after air annealing at 400 °C for 3 min. (*C*) The normalized height histogram of an oxidized biflake, marked by an orange square in (*A*). The Gaussian fit (solid black curve) represents the height of the biflake, while the extended tail at higher heights indicates the height distribution of TiO_2 nanoparticles. This tail distribution can be fitted by a Lognormal function as shown in the *Inset*, upon the subtraction of the Gaussian fit from the height histogram. (*D*) The normalized height histogram of a biflake marked by a purple square in (*B*). The histogram fits well to a single Gaussian function (solid black curve) without an extended tail indicating the absence of TiO_2 nanoparticles. (*E*) The root mean square (RMS) roughness (*Left* axis) of monoflake (red) and biflake (gray) MXenes, and the average height of TiO_2 nanoparticles (orange, *Right* axis) for vacuum annealed samples at various temperatures, after air annealing at 400 °C for 3 min. (*F*) Resistivity vs. temperature of the Vacuum-600 °C-2 h $Ti_3C_2T_x$ film on a Si substrate, measured with in situ SE during consecutive thermal cycling in air at 10 °C/min to 200 °C (gray curve), 300 °C (pink curve), and 400 °C (blue curve), with a 3-min hold time at each temperature.

discrepancy, it is important to consider the availability and the source of water and oxygen in each case. For an As-prepared monoflake, water molecules can be either adsorbed on the flake surface (43) or be trapped between the MXene flake and its supporting substrate (27, 29), which is native silicon oxide for most samples studied here. The absence of oxidation in $Ti_3C_2T_x$ monoflakes, even for the stoichiometric MXene with more internal defects (*SI Appendix*, Fig. S8), indicates that the surface and substrate adsorbed H_2O evaporate below the oxidation onset temperature (300 °C, in Fig. 1*A*) in air. This hypothesis is supported by previous reports that show a 100 °C onset of H_2O desorption (21, 23) and breakdown of $OH-H_2O$ complexes (43) in $Ti_3C_2T_x$. A similar desorption onset is also measured on silica surfaces (44). In contrast, in stacked flakes water can also be trapped in the interflake space (21, 22, 45), as schematically shown in Fig. 2. The trapped water, which can be physically adsorbed or chemically confined, e.g., through hydrogen bonding (46), locally oxidizes the MXene to form TiO_2 nanoparticles, at elevated temperatures above 300 °C in air. The oxidation mechanism involving confined water could potentially be similar to the proposed degradation route in aqueous solutions, which is predominantly through hydrolysis (18). If so, it is expected that methane would also be produced as a reaction product, the production of which can be investigated in the future to confirm this hypothesis. This hypothesis can explain why increasing the number of stacking results in more and larger TiO_2 nanoparticles (*SI Appendix*, Fig. S14) while increasing vacuum annealing temperature reduces the average number and size of TiO_2 nanoparticles (Fig. 3*E*) due to the reduce of the amount of confined water through evaporation. These results also imply that, while some water evaporates upon vacuum annealing at moderate temperatures, confined water does not fully evaporate unless vacuum annealing is performed at 600 °C for 2 h (schematically shown in Fig. 2), where stacked flakes are finally stabilized under air annealing.

The Kinetics and Thermodynamics of Confined Water Removal. It is rather challenging to quantify trapped (physically adsorbed) and confined (chemically attached) water in the interflake region. However, these two types of water appear to have distinct morphological signatures in AFM imaging. Fig. 4 *A–C* illustrate high-resolution AFM topography images of biflake surfaces for As-prepared, Vacuum-200 °C-24 h, and Vacuum-600 °C-2 h films on atomically flat mica substrates (used to reduce the role of substrate roughness in these measurements). The surfaces of the As-prepared biflakes show a rough morphology with semi-interconnected islands with an approximate height of 0.30 ± 0.14 nm. This can be seen in the line profile shown in Fig. 4*A* (0.36 nm height difference) as well as the two distinct height distributions observed in the corresponding height histogram (*SI Appendix*, Fig. S16*A*, 0.3 ± 0.14 nm peak to peak distance). The height difference is consistent with the thickness of a submonolayer of water being trapped between the two flakes, similar to previous observations of water trapped between graphene and mica substrate (0.37 nm) (47). Given the mixed termination of MXenes, this water likely exists in regions with −OH and −O terminations. The island structure is absent on the monoflake surfaces of these films (*SI Appendix*, Fig. S17) showing that a minimal amount of water is trapped between the monoflakes and the substrate. Upon vacuum annealing, the island structure is suppressed on biflake surfaces of Vacuum-200 °C-24 h, and completely absent on the surface of the Vacuum-600 °C-2 h film. The height histograms of these surfaces only show a single Gaussian distribution indicating their dramatically reduced number of trapped water (*SI Appendix*, Fig. S16 *A–C*), consistent with the single Gaussian distribution of the height histograms of these monoflake surfaces (*SI Appendix*, Fig. S16 *D–F*). As such, one can conclude most of the trapped H_2O molecules can be removed upon vacuum annealing at 200 °C for 24 h, which is in line with previous thermogravimetric analysis (TGA) and SE results (16, 23). However, −OH and −O terminations can be stable up to above 400 °C in vacuum (21, 48), meaning that more strongly bonded water could persist on these samples even after 500 °C vacuum annealing, causing air oxidation in stacked flakes as shown in *SI Appendix*, Fig. S13*C*.

To further confirm water removal after vacuum annealing, X-ray diffraction analysis (XRD) was performed. The detailed XRD results of As-prepared (red curve), Vacuum-200 °C-24 h (orange curve), and Vacuum-600 °C-2 h (purple curve) $Ti_3C_2T_x$ MXene films (~5 nm thickness) deposited on Si substrate are shown in *SI Appendix*, Fig. S18. No TiO_2 peaks are observed

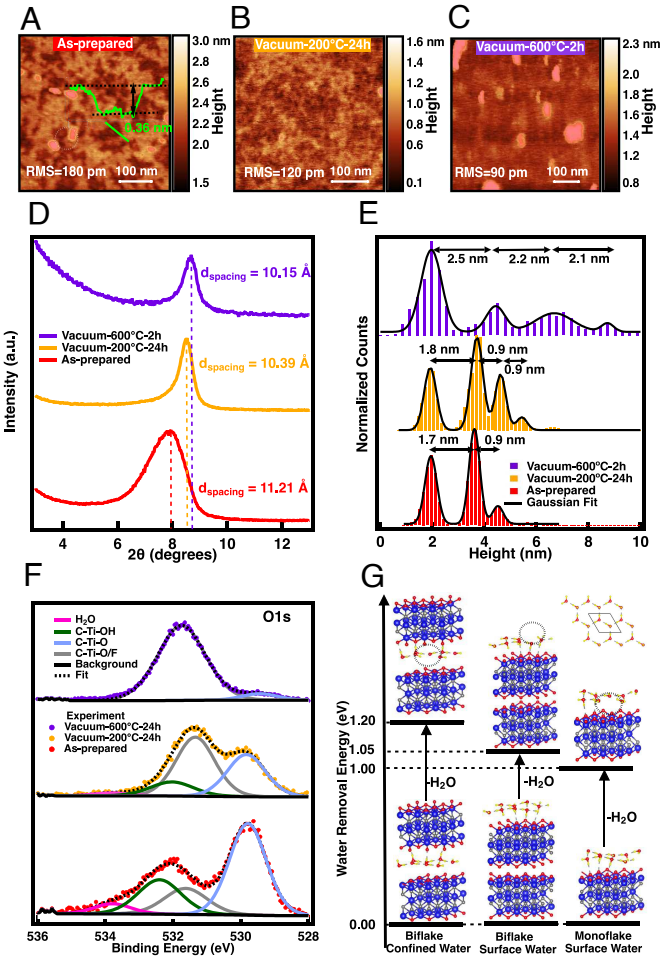

Fig. 4. Removal barriers for trapped and confined interflake water in $Ti_3C_2T_x$ MXene. (*A–C*) High-resolution AFM images of biflake surfaces in As-prepared, Vacuum-200 °C-24 h, and Vacuum-600 °C-2 h $Ti_3C_2T_x$ films on mica substrates. The *Inset* in (*A*) is the height profile along the green line, representing the height change due to the presence of water. (*D*) XRD (002) peaks of As-prepared (red curve), Vacuum-200 °C-24 h (orange curve), and Vacuum-600 °C-2 h (purple curve) $Ti_3C_2T_x$ MXene films (~5 nm thickness) deposited on Si substrate. The 2θ peak values are 7.78 ± 0.79 degrees for As-prepared, 8.50 ± 0.26 degrees for Vacuum-200 °C-24 h, and 8.64 ± 0.27 degrees for Vacuum-600 °C-2 h, where the error represents the width of each peak. The peak shift to higher 2θ represents a decrease in the apparent interlayer spacing. (*E*) Normalized height histogram of As-prepared (red bar), Vacuum-200 °C-24 h (orange bar), and Vacuum-600 °C-2 h (purple bar) films based on the AFM images shown in *SI Appendix*, Fig. S9 *A*, *B*, and *D*. Four Gaussian functions were used to fit each histogram (solid black curves), representing from *Left* to *Right*, the silicon substrate, monoflake, biflake, and triflake height distributions in each image. The peak-to-peak distances, shown in black arrows, indicate the thicknesses of the first to third flakes, from *Left* to *Right*. (*F*) The O 1s XPS spectra of As-prepared (red dots), Vacuum-200 °C-24 h (orange dots), and Vacuum-600 °C-2 h (purple dots) films coated on Si substrate. The fitting details for each peak can be found in *SI Appendix*, Note S2 and Tables S2, S5, and S6. (*G*) DFT-calculated removal energies for the first water molecule at different configurations. The zero-energy structures are the relaxed structures of a 3 × 3 $Ti_3C_2O_2$ system with a confined or surface water layer containing eight water molecules per repeat unit. The *Top* row shows the corresponding energies and relaxed structures of a 3 × 3 $Ti_3C_2O_2$ system with seven water molecules per repeat unit, and the dashed circles show the site of the first removed water. The *Top Right* corner *Inset* shows the crystal structure of the hexagonal water monolayer. Color code: Ti (blue), C (gray), O (red), and H (yellow).

in these XRD results, suggesting that no detectable oxidation occurred after 600 °C vacuum annealing. The higher-resolution data around the (002) peaks in these samples are shown in Fig. 4*D*. The (002) peak shifts dramatically to higher 2θ values after 200 °C vacuum annealing indicating a decrease in the apparent interlayer spacing from 11.21 Å for As-prepared to 10.39 Å for Vacuum-200 °C-24 h, consistent with the water morphology change observed in AFM measurements (Fig. 4 *A–C*). The (002) peak further shifts slightly after 600 °C vacuum annealing to an apparent interlayer spacing of 10.15 Å. This observation is consistent with the previously reported XRD results of thick Vacuum-annealed $Ti_3C_2T_x$ films. (21, 49, 50) However, the height profiles in *SI Appendix*, Fig. S9 *E* and *F* and the height histograms in Fig. 4*E* (based on the AFM images in *SI Appendix*, Fig. S9 *A*, *B*, and *D*) show a contrasting change with a systematic increase in the distance between the distributions corresponding to the substrates, first, second, and third flakes upon vacuum annealing to 600 °C. To understand this apparent discrepancy between interlayer distance changes in XRD and the height measurements of AFM, it is worth highlighting the differences in the measured quantity of each technique. XRD measurements are performed globally on the entire sample and require coherent reflection of the X-ray beam, meaning that areas with perfectly parallel structures near the surface of the flakes can produce a stronger signal, while the more disordered edges of the samples and regions with high roughness will not contribute to the signal. In these areas, the removal of water reduces the interflake distance, as can be seen for the 200 °C vacuum anneal sample in Fig. 4*B*. However, while AFM is a more local technique, it can capture every difference in sample height, including the edges and rough regions, where the flakes are no longer parallel, resulting in an average increased distance as well as a broadening of each peak in the height histogram (Fig. 4*E*). The broadening in height histogram peaks indicates increased heterogeneity, meaning that a large portion of the sample will not contribute to the XRD data. In addition, SE measurements also corroborate the average height increase in Vacuum-600 °C-2 h films (*SI Appendix*, Fig. S19). More details of SE measurements can be found in *SI Appendix*, Note S6.

The thickness increase upon vacuum annealing at 600 °C can be attributed to chemical changes upon the removal of the confined H_2O, which was further confirmed by the O 1s XPS spectra shown in Fig. 4*F*. The H_2O percentage decreases from 6% (As-prepared) to 1.7% (Vacuum-200 °C-24 h), and vanishes for Vacuum-600 °C-2 h samples. In addition to water, the C−Ti−OH peak also vanishes and the two C−Ti−O peaks increase after vacuum annealing at 600 °C-2 h, indicating that the −OH terminations have converted to −O terminations at high temperature (14). The two peaks centered at 529 eV and 532 eV, representing the −O terminations that reside on two different sites. Annealing at high temperature allows the transfer of −O and −F terminations from one site to another, changing the relative intensity of these two peaks. This is consistent with previous results. (32, 51) The other XPS spectra (Ti 2p and C 1s) are not significantly affected by annealing at 600 °C in vacuum. These results can be found in *SI Appendix*, Fig. S10. The chemical changes of the surface terminations were further confirmed by water droplet contact angle measurements (*SI Appendix*, Fig. S20).

The contact angle increases slightly from As-prepared to Vacuum-200 °C-24 h film, but both samples are still hydrophilic. This suggests that −O and −OH surface terminations are still present in these samples and the trapped water has not been completely removed at this stage. This is in line with the previous work, which demonstrated that partial water is still present after 200 °C anneal. (26) After 600 °C-2 h vacuum anneal, the contact angle increases dramatically to 100 °, indicating hydrophobic surface properties of the film. This suggests that the chemical

properties are modified after confined water removal, likely due to the removal of −OH terminations, which is also consistent with the XPS results (Fig. 4*F*). The removal of hydrogen bonding or other chemical bonds can reduce the interflake adhesion energy, thus increasing their equilibrium distances. Water bridging has been previously speculated as the reason for higher interflake adhesion energy (52). For $Ti_3C_2T_x$/$Ti_3C_2T_x$, adhesion energy of 1.23 J/m^2 has been reported, which is higher than 0.9 J/m^2 reported for $Ti_3C_2T_x$ and silicon substrate (52, 53), explaining the observed thickness differences in the first and second flakes (Figs. 1 and 4).

To further understand the effects of confined water on stacked flakes oxidation, DFT calculations were performed to calculate the removal energy of H_2O from monoflake and biflake $Ti_3C_2T_x$ MXenes (*Materials and Methods*). These calculations first demonstrated that the −O termination is the most thermodynamically stable one under a wide range of experimental conditions, consistent with previous studies (54). More calculation procedures and results can be found in *SI Appendix*, Note S7 and Table S8. Therefore, the $Ti_3C_2O_2$ was chosen to calculate the H_2O binding energies. To compare the removal energies of confined and surface water, a hexagonal water monolayer (*Top Right Inset* of Fig. 4*G*) was used (*SI Appendix*, Note S8).

It was found that the removal energy of a single water molecule is 1.20 eV for confined water and 1.05 eV for surface water, indicating that it is more difficult to remove confined water than surface water from the biflake $Ti_3C_2O_2$, as shown in Fig. 4*H*, qualitatively consistent with the experimental observations. The removal energy of surface water on monoflake $Ti_3C_2O_2$ was also calculated to be 1.00 eV, similar to that for surface water on biflake $Ti_3C_2O_2$, consistent with the vdW interaction between the $Ti_3C_2O_2$ flakes. The bench-marking details of the water removal energy are in *SI Appendix*, Notes S9 and S10. In addition to the hexagonal confined water model, the H_2O removal energy from a zigzag water monolayer (with different concentrations) was also calculated. These results also demonstrate that the confined water has higher removal energy compared to the surface water. More details can be found in *SI Appendix*, Note S9 and Fig. S21 and Table S7. Despite the fact that the water monolayer could possess various structural configurations, it was demonstrated that the removal energy of confined water is always higher than that of the surface water.

Conclusions

Contrary to the conventional wisdom, we found that upon proper annealing in air, $Ti_3C_2T_x$ MXene monoflakes are exceptionally stable, up to 600 °C, while multiflakes are readily oxidized above 300 °C. We demonstrated that the oxidation of multiflake $Ti_3C_2T_x$ is due to confined water, which can be suppressed significantly when the films are vacuum annealed at elevated temperatures; specifically, multiflakes become thermally stable upon vacuum annealing at 600 °C allowing them to withstand 600 °C in air. We propose that the interflake confined water, with higher removal energy relative to the surface water, is the main reason for the multiflake susceptibility to oxidation. Our work not only demonstrates the higher thermal stability of monoflakes $Ti_3C_2T_x$ but also sheds light on the nature of the lower threshold for biflake oxidation, which is important both from a fundamental point of view in understanding MXene interfaces and their role in MXene stability as well as facilitating their use in future applications at extremely high temperatures.

Materials and Methods

Synthesis of Ti_3AlC_2 MAX. Optimized Ti_3AlC_2 MAX phase was synthesized by combining titanium carbide, titanium, and aluminum in the molar ratio of 2:1.25:2.2 molar (55). Subsequently, the mixture was jar-milled in Nalgene high-density polyethylene bottles along with yttria-stabilized zirconia balls (ball-to-powder mass ratio of 2:1) for 18 h at 64 RPM. The jar-milled powders were packed into an alumina crucible, covered with graphite foil, and placed in a high-temperature tube furnace (Carbolite Gero, 1700 °C model) for reactive pressureless sintering. Before starting the heating cycle, the furnace was purged with argon (99.999% purity) for 20 min. Subsequently, it was subjected to a controlled heating process, gradually raising the temperature to 1400 °C with a steady heating rate of 3.5 °C/min, and 4 h dwell, ensuring an uninterrupted flow of argon. Following the 4-h sintering process, the furnace was gradually cooled down to room temperature at a controlled rate of 10 °C/min. The sintered block was milled into a fine powder (<71 μm) using a TiN-coated mill bit. For stoichiometric Ti_3AlC_2 MAX, which was used for the synthesis of stoichiometric $Ti_3C_2T_x$ MXene (*SI Appendix*, Fig. S8), the titanium carbide, titanium, and aluminum powders were mixed in a 2:1:1 molar ratio, but the synthesis was otherwise the same.

Synthesis of $Ti_3C_2T_x$ MXene. The detailed synthesis procedures can be found in our previous work (31). Briefly, For $Ti_3C_2T_x$ MXene synthesis, 1 g of optimized Ti_3AlC_2 MAX was first washed using 10 mL of 9 M hydrochloric acid (HCl) for 18 h to remove the intermetallic impurities, and then mixed with an etchant solution (6:3:1 mixture (by volume) of 12 M HCl, deionized (DI) water, and 28.4 M hydrofluoric acid (HF) and stirred at 400 RPM for 24 h at 35 °C. The etched $Ti_3C_2T_x$ MXene was washed with deionized water via repeated centrifugation at 3234 relative centrifugal force (RCF, four to five cycles with ∼200 mL of deionized water) until the supernatant reached pH ∼6. For delamination, the etched multilayered $Ti_3C_2T_x$ MXene sediment (typically 50 mL/per gram of starting etched powder) was then added to 0.5 M LiCl solution. The mixture of lithium chloride (LiCl) and etched multilayered $Ti_3C_2T_x$ MXene was then stirred at 400 RPM for 1 h at 65 °C under constant argon flow. The mixture was then washed with deionized water via centrifugation at 3234 RCF for 5, 10, 15, and 20 min. The final mixture was then vortexed for 30 min followed by centrifugation at 2380 RCF for 30 min to ensure the MXene solutions only contained single-to-few-layered flakes. The final suspension of $Ti_3C_2T_x$ MXene was collected and stored in a freezer at −20 °C until use.

Fabrication of $Ti_3C_2T_x$ Films. Different thickness films were spun-cast from the aqueous solution (0.5 to 10 mg/mL) on a Si substrate (500 ± 25 μm thick, p-type boron-doped, 0.01 to 0.05 ohm.cm, Virginia Semiconductor) and freshly cleaved mica (Hi-grade V2, Ted Pella, Inc.) substrates. Si substrates were first cleaned with acetone, ethanol, and deionized (DI) water. After drying with nitrogen gas, the substrates were exposed to oxygen plasma for 10 min. The mica substrates were directly used after mechanical exfoliation. All colloidal solutions were bath-sonicated for 2 min before spin-coating. Typically, films were constructed on 4 cm^2 substrates using a 100 μL solution via a two-step spin-casting (Laurell WS 400BZ-6NPP/Lite spin coater) process by spinning at 500 revolutions-per-minute (RPM) for 60 s, followed by 2,000 RPM for 10 s.

Vacuum Annealing and Air Annealing Treatments. The schematic of the designed experimental approach is shown in Fig. 2. Briefly, As-prepared and Vacuum-annealed MXene films were used for the air annealing (oxidation test) treatment. For vacuum annealing treatment at 200 °C, MXene films were placed in an aluminum foil boat, then annealed in a vacuum oven (base pressure: <10 mTorr) for 24 h. For 500 °C and 600 °C vacuum annealing, the samples were mounted onto a temperature-controlled Linkam stage (THMS600) inside a custom vacuum chamber (base pressure: 20 to 40 mTorr) and held at each temperature for the desired length of time. The samples were then cooled to room temperature prior to other measurements.

For air annealing, the samples were mounted onto the temperature-controlled Linkam stage in ambient conditions. For each step of the oxidation test, the temperature was increased at a rate of either 10 or 60 °C/min to the set temperature, held constant for various durations, and then cooled down to room

temperature at the same rate. For example, for the data shown in *SI Appendix*, Fig. S1*C* (red curve), the set temperatures and durations are 75 °C, 1 min, 125 °C, 1 min, 200 °C, 1 min, 300 °C, 3 min, and 400 °C 3 min, respectively. For convenience, the sample after vacuum and air annealing treatment are denoted as Vacuum-T-t and Air-T-t, where "T" and "t" are the annealing temperature and time, respectively. The pristine sample is denoted as As-prepared.

Spectroscopic Ellipsometry Measurements. The spectroscopic ellipsometer (SE) used in this study was an M-2000 instrument (J. A. Woollam), with a wavelength range of 371 nm to 1687 nm (0.73 eV to 3.34 eV). For in situ experiments, the incident angle was fixed at 70 °. MXene films were mounted onto a temperature-controlled Linkam stage and heated from 25 °C to 600 °C either under ambient conditions (air, with typical 10 to 20% humanity) or vacuum (base pressure: 20 to 40 mTorr) with heating rates of either 10 °C/min or 60 °C/min. The desired temperatures and heating rates were controlled by the Linksys software. The sampling rate of in situ SE measurements was 1 s with high-accuracy zone averaging. The SE results were modeled using CompleteEase software (version 6.69) package. More details about the data modeling and results can be found in *SI Appendix*, Note S1 and Fig. S1 and Table S1.

AFM Imaging. AFM was carried out in tapping mode using a Bruker Icon AFM (Bruker) instrument equipped with a closed-loop scanner. Tapping mode AFM Probes with Aluminum Reflective Coating (Budget Sensors, Tap300Al-G, resonance frequency ∼300 kHz, tip radius ∼10 nm) were used to record topography images with 512 × 512-pixel resolution. For high-resolution images, high-resolution silicon AFM probes (Budget Sensors, SHR150, resonance frequency ∼150 kHz, tip radius ∼1 nm) were used. Topography images were obtained in open-loop mode with 512 × 512-pixel resolution. AFM images were processed and analyzed by Gwyddion software. A third-order polynomial was employed to flatten the background for topography images. Height histograms and line profiles were extracted and analyzed after the flattening process.

PF-KPFM Measurements. Pulsed force Kelvin probe force microscopy (PF-KPFM) experiments were performed using a home-made lock-in-based setup (56). Briefly, a Multimode 8 AFM instrument (Bruker) with a sharp platinum-coated AFM tip with a radius of approximately 30 nm (MikroMasch NSC:15/pt), a custom PF-KPFM triggering circuit, and a lock-in amplifier (MFLI-MD-PID, Zurich Instruments) were used. The operational principle of KPFM is through the alignment of the Fermi level between two dissimilar metals or semiconductors in close proximity, in which electrons flow and generate a contact potential (56). KPFM exploits this effect by using an AFM tip as a reference with a defined work function to measure an unknown sample at the nanoscale. PF-KPFM is a new variant of KPFM that utilizes the pulsed force mode (peak force tapping mode) and a field effect transistor (FET) to switch the electrical connectivity for KPFM measurements (56), in order to improve the instrument's spatial resolution under ambient conditions. During the PF-KPFM measurements, the AFM tip intermittently touched the sample at a frequency of ∼4 kHz under the peak force tapping mode. Shortly after the tip detached from the sample (when the tip-sample distance was between 1 to 3 nm), a FET served as a fast switch, connecting and disconnecting the tip and sample multiple times at the cantilever resonance frequency. This process induces periodic Coulombic forces that match the cantilever's free space resonant oscillation period. The oscillation amplitude is dependent on the surface potential of the sample due to the contact potential difference. The amplitude of this oscillation was compensated for or suppressed by applying a direct voltage (VDC) between the tip and the sample. The magnitude of the external VDC needed to suppress the oscillations correlates to the contact potential difference at each point of the sample beneath the tip. With the aid of a proportional-integral-derivative (PID) controller embedded in a Lock-in amplifier (MFLI-MD-PID, Zurich Instruments), this external VDC was recorded by the AFM controller to map the surface potential of the sample. The topography and surface potential images were obtained with 256 × 256-pixel resolution. Gwyddion software was used to proceed with the data analysis, similar to the approach described for AFM image analysis.

XPS Measurements. XPS measurements were performed using a Physical Electronics (PHI) VersaProbe 5000 instrument (Physical Electronics) with a 200 μm and 50 W monochromatic Al-Kα (1486.6 eV) X-ray source. Charge neutralization was achieved by a dual-beam system involving low-energy Ar^+ ions and low-energy electrons at 1 eV and 200 μA. Survey spectra were collected with a pass energy of 117.4 eV and an energy resolution of 0.5 eV. High-resolution F 1s, O 1s, Ti 2p, and C 1s spectra were collected with a pass energy of 23.5 eV and an energy resolution of 0.05 eV. The $Ti_3C_2T_x$ C 1s peak at 282.00 eV was used for binding energy scale correction, which was less than 0.10 eV for both samples due to their conducting nature and sufficient charge compensation. CasaXPS V2.3.25PR1.0 was utilized for peak fitting and quantification. More details about data analysis are found in *SI Appendix*, Note S2 and Figs. S3 and S10 and Tables S2–S6.

XRD Measurements. XRD patterns were analyzed using a Bruker D8 X-ray diffractometer with a Cu Kα (λ= 1.5406 Å) emitter and a Lynxeye detector. A corundum standard was used to ensure each detector was calibrated. The samples were mounted on Kapton tapes and scanned from 5 ° to 80 ° with a step size of 0.02 °.

Contact Angle Measurements. The contact angle of water droplet on the MXene flakes was measured by a goniometer (Attention, KSV Instruments, Inc.) A 2 μL deionized water droplet was pipetted onto the MXene surface for the measurements.

DFT Calculations. DFT calculations were performed using the Vienna Ab initio Simulation Package (57, 58). Projector-augmented wave pseudopotentials were implemented, where for Ti atoms the valence 3d and semicore 4s electrons were included, and for C, O, and H atoms only valence electrons were included. Calculations were performed under the spin-polarized DFT+U formalism in order to capture the strong correlation effects of Ti 3d electrons. To determine the effective value U_{eff}, the magnetic moments of monolayer $Ti_3C_2O_2$ at different U_{eff} were compared with the results from hybrid functional HSE06 calculations (59); and were determined to be $U_{\text{eff}} = 3$ eV. For all other calculations, the GGA-PBE functional was used. Furthermore, the DFT-D3 method was also used with Becke–Johnson damping to describe the vdW interactions (60). For all calculations, the **k**-points were sampled using a grid with density $0.03 \times 2\pi$ Å^{-1}, and 600 eV was used for the kinetic energy cutoff of the plane-wave basis sets. For geometry optimization, the force convergence criterion of 0.005 eV/Å, and a vacuum of thickness of 20 Å were used.

Data, Materials, and Software Availability. All study data included in the article and *SI Appendix* are available on Open Science Framework (https://doi.org/10.17605/OSF.IO/GWPDV) (61).

ACKNOWLEDGMENTS. H.F., A.T., Z. Fang, V.R., A.A.S., C.P., M.S., A.M.R., B.A., and Z. Fakhraai acknowledge funding support from the US NSF, award number CMMI-2134607. A.Z. and X.G.X. would like to thank support from the US NSF, award number CHE-1847765. Z. Fang acknowledges funding from the NSF, award number CHE-2023644, for computational modeling of water influencing MXene interlayer spacings. H.F. acknowledges the School of Arts and Sciences at the University of Pennsylvania for the Postdoctoral Fellowship. A.A.S was supported with a postdoctoral fellowship from the Vagelos Institute of Energy Science and Technology. We would like to thank Prof. Daeyeon Lee and Dr. Paradorn Rummaneethorn from the University of Pennsylvania for help with contact angle measurements.

Author affiliations: [a]Department of Chemistry, University of Pennsylvania, Philadelphia, PA 19104; [b]School of Materials Engineering, Purdue University, West Lafayette, IN 47907; [c]Department of Mechanical and Energy Engineering and Integrated Nanosystems Development Institute, Indiana University-Purdue University Indianapolis, Indianapolis, IN 46202; [d]Department of Chemistry, Lehigh University, Bethlehem, PA 18015; [e]Department of Chemical and Biological Engineering, Drexel University, Philadelphia, PA 19104; and [f]School of Mechanical Engineering, Purdue University, West Lafayette, IN 47907

1. X. Li *et al*., MXene chemistry, electrochemistry and energy storage applications. *Nat. Rev. Chem.* **6**, 389–404 (2022).
2. B. Anasori, M. R. Lukatskaya, Y. Gogotsi, 2D metal carbides and nitrides (MXenes) for energy storage. *Nat. Rev. Mater.* **2**, 1–17 (2017).
3. K. Hantanasirisakul *et al*., Fabrication of $Ti_3C_2T_x$ MXene transparent thin films with tunable optoelectronic properties. *Adv. Electron. Mater.* **2**, 1600050 (2016).
4. F. Shahzad *et al*., Electromagnetic interference shielding with 2D transition metal carbides (MXenes). *Science* **353**, 1137–1140 (2016).
5. B. Lyu *et al*., Large-area MXene electrode array for flexible electronics. *ACS Nano* **13**, 11392–11400 (2019).
6. J. A. Kumar *et al*., Methods of synthesis, characteristics, and environmental applications of MXene: A comprehensive review. *Chemosphere* **286**, 131607 (2022).
7. G. P. Lim *et al*., Cytotoxicity of MXene-based nanomaterials for biomedical applications: A mini review. *Environ. Res.* **201**, 111592 (2021).
8. M. Naguib *et al*., Two-dimensional nanocrystals produced by exfoliation of Ti_3AlC_2. *Adv. Mater.* **23**, 4248–4253 (2011).
9. Y. Gogotsi, B. Anasori, The rise of MXenes. *ACS Nano* **13**, 8491–8494 (2019).
10. A. VahidMohammadi, J. Rosen, Y. Gogotsi, The world of two-dimensional carbides and nitrides (MXenes). *Science* **372**, eabf1581 (2021).
11. K. R. G. Lim *et al*., Fundamentals of MXene synthesis. *Nat. Synth.* **1**, 601–614 (2022).
12. A. Lee, M. Shekhirev, M. Anayee, Y. Gogotsi, Multi-year study of environmental stability of $Ti_3C_2T_x$ MXene films. *Graphene and 2D Mater.* **9**, 77–85 (2024).
13. H. Ghassemi *et al*., In situ environmental transmission electron microscopy study of oxidation of two-dimensional Ti_3C_2 and formation of carbon-supported TiO_2. *J. Mater. Chem. A* **2**, 14339–14343 (2014).
14. F. Cao *et al*., Recent advances in oxidation stable chemistry of 2D MXenes. *Adv. Mater.* **34**, 2107554 (2022).
15. T. Habib *et al*., Oxidation stability of $Ti_3C_2T_x$ MXene nanosheets in solvents and composite films. *NPJ 2D Mater. Appl.* **3**, 1–6 (2019).
16. M. Seredych *et al*., High-temperature behavior and surface chemistry of carbide MXenes studied by thermal analysis. *Chem. Mater.* **31**, 3324–3332 (2019).
17. F. Xia *et al*., Ambient oxidation of Ti_3C_2 MXene initialized by atomic defects. *Nanoscale* **11**, 23330–23337 (2019).
18. S. Huang, V. N. Mochalin, Hydrolysis of 2D transition-metal carbides (MXenes) in colloidal solutions. *Inorg. Chem.* **58**, 1958–1966 (2019).
19. H. Wang *et al*., Enhancement of the electrical properties of MXene Ti_3C_2 nanosheets by post-treatments of alkalization and calcination. *Mater. Lett.* **160**, 537–540 (2015).
20. N. Liu *et al*., High-temperature stability in air of $Ti_3C_2T_x$ MXene-based composite with extracted bentonite. *Nat. Commun.* **13**, 1–10 (2022).
21. J. L. Hart *et al*., Control of MXenes' electronic properties through termination and intercalation. *Nat. Commun.* **10**, 1–10 (2019).
22. M. Ghidiu, S. Kota, V. Drozd, M. W. Barsoum, Pressure-induced shear and interlayer expansion in Ti_3C_2 MXene in the presence of water. *Sci. Adv.* **4**, eaao6850 (2018).
23. A. A. Shamsabadi *et al*., The evolution of MXenes conductivity and optical properties upon heating in air. *Small Methods* **7**, 2300568 (2023).
24. C. Zhang *et al*., Transparent, flexible, and conductive 2D titanium carbide (MXene) films with high volumetric capacitance. *Adv. Mater.* **29**, 1702678 (2017).
25. M. Carey *et al*., Dispersion and stabilization of alkylated 2D MXene in nonpolar solvents and their pseudocapacitive behavior. *Cell Rep. Phys. Sci.* **1**, 100042 (2020).
26. Y. Lee *et al*., Oxidation-resistant titanium carbide MXene films. *J. Mater. Chem. A* **8**, 573–581 (2020).
27. A. Lipatov *et al*., Effect of synthesis on quality, electronic properties and environmental stability of individual monolayer Ti_3C_2 MXene flakes. *Adv. Electron. Mater.* **2**, 1600255 (2016).
28. P. Pendyala, J. Lee, S. J. Kim, E.-S. Yoon, Layer-dependent frictional properties of $Ti_3C_2T_x$ MXene nanosheets. *Appl. Surf. Sci.* **603**, 154402 (2022).
29. A. Lipatov *et al*., Elastic properties of 2D $Ti_3C_2T_x$ MXene monolayers and bilayers. *Sci. Adv.* **4**, eaat0491 (2018).
30. A. Sarycheva, M. Shanmugasundaram, A. Krayev, Y. Gogotsi, Tip-enhanced raman scattering imaging of single-to few-layer $Ti_3C_2T_x$ MXene. *ACS Nano* **16**, 6858–6865 (2022).
31. A. Thakur *et al*., Step-by-step guide for synthesis and delamination of $Ti_3C_2T_x$ MXene. *Small Methods* **7**, 2300030 (2023).
32. V. Natu *et al*., A critical analysis of the X-ray photoelectron spectra of $Ti_3C_2T_z$ MXenes. *Matter* **4**, 1224–1251 (2021).
33. P. Serles *et al*., Friction of $Ti_3C_2T_x$ MXenes. *Nano Lett.* **22**, 3356–3363 (2022).
34. M. Naguib *et al*., One-step synthesis of nanocrystalline transition metal oxides on thin sheets of disordered graphitic carbon by oxidation of MXenes. *Chem. Commun.* **50**, 7420–7423 (2014).
35. J. Choi *et al*., In situ formation of multiple schottky barriers in a Ti_3C_2 MXene film and its application in highly sensitive gas sensors. *Adv. Func. Mater.* **30**, 2003998 (2020).
36. M. Ghidiu, M. R. Lukatskaya, M.-Q. Zhao, Y. Gogotsi, M. W. Barsoum, Conductive two-dimensional titanium carbide 'clay' with high volumetric capacitance. *Nature* **516**, 78–81 (2014).
37. A. Lipatov *et al*., Electrical and elastic properties of individual single-layer $Nb_4C_3T_x$ MXene flakes. *Adv. Elect. Mater.* **6**, 1901382 (2020).
38. T. Schultz *et al*., Surface termination dependent work function and electronic properties of $Ti_3C_2T_x$ MXene. *Chem. Mater.* **31**, 6590–6597 (2019).
39. V. Mansfeldova *et al*., Work function of TiO_2 (anatase, rutile, and brookite) single crystals: Effects of the environment. *J. Phys. Chem. C* **125**, 1902–1912 (2021).
40. P. P. Michałowski *et al*., Oxycarbide MXenes and MAX phases identification using monoatomic layer-by-layer analysis with ultralow-energy secondary-ion mass spectrometry. *Nat. Nanotechnol.* **17**, 1192–1197 (2022).
41. Y.-C. Lin, H. Komatsu, J. Ma, P. H. Axelsen, Z. Fakhraai, Quantitative analysis of amyloid polymorphism using height histograms to correct for tip convolution effects in atomic force microscopy imaging. *RSC Adv.* **6**, 114286–114295 (2016).
42. H. Fang *et al*., Ag nanoplatelets as efficient photosensitizers for TiO_2 nanorods. *J. Chem. Phys.* **156**, 024703 (2022).
43. W. Zaman *et al*., In situ investigation of water on MXene interfaces. *Proc. Natl. Acad. Sci. U.S.A.* **118**, e2108325118 (2021).
44. J. Trébosc, J. W. Wiench, S. Huh, V.S.-Y. Lin, M. Pruski, Solid-state NMR study of MCM-41-type mesoporous silica nanoparticles. *J. Am. Chem. Soc.* **127**, 3057–3068 (2005).
45. H. Minmin *et al*., Surface functional groups and interlayer water determine the electrochemical capacitance of $Ti_3C_2T_x$ MXene. *ACS Nano* **12**, 3578–3586 (2018).
46. T. Kobayashi *et al*., Nature of terminating hydroxyl groups and intercalating water in $Ti_3C_2T_x$ MXenes: A study by 1H solid-state NMR and DFT calculations. *J. Phys. Chem. C* **124**, 13649–13655 (2020).
47. X. Ke, P. Cao, J. R. Heath, Graphene visualizes the first water adlayers on mica at ambient conditions. *Science* **329**, 1188–1191 (2010).
48. Z. Wang *et al*., Unraveling and regulating self-discharge behavior of $Ti_3C_2T_x$ MXene-based supercapacitors. *ACS Nano* **14**, 4916–4924 (2020).
49. J. T. Lee *et al*., Covalent surface modification of $Ti_3C_2T_x$ MXene with chemically active polymeric ligands producing highly conductive and ordered microstructure films. *ACS Nano* **15**, 19600–19612 (2021).
50. M. Lounasvuori, T. Zhang, Y. Gogotsi, T. Petit, Tuning the microenvironment of water confined in $Ti_3C_2T_x$ MXene by cation intercalation. *J. Phys. Chem. C* **128**, 2803–2813 (2024).
51. I. Persson *et al*., On the organization and thermal behavior of functional groups on Ti_3C_2 MXene surfaces in vacuum. *2D Mater.* **5**, 015002 (2017).
52. Y. Li *et al*., Adhesion between MXenes and other 2D materials. *ACS Appl. Mater. Interfaces* **13**, 4682–4691 (2021).
53. Y. Li, S. Huang, C. Wei, W. Chenglin, V. N. Mochalin, Adhesion of two-dimensional titanium carbides (MXenes) and graphene to silicon. *Nat. Commun.* **10**, 3014 (2019).
54. H. Tao *et al*., Chemical origin of termination-functionalized MXenes: $Ti_3C_2T_2$ as a case study. *J. Phys. Chem. C* **121**, 19254–19261 (2017).
55. T. S. Mathis *et al*., Modified MAX phase synthesis for environmentally stable and highly conductive Ti_3C_2 MXene. *ACS Nano* **15**, 6420–6429 (2021).
56. A. Zahmatkeshsaredorahi, D. S. Jakob, H. Fang, Z. Fakhraai, G. X. Xiaoji, Pulsed force kelvin probe force microscopy through integration of lock-in detection. *Nano Lett.* **23**, 8953–8959 (2023).
57. G. Kresse, J. Hafner, Ab initio molecular dynamics for liquid metals. *Phys. Rev. B* **47**, 558 (1993).
58. G. Kresse, J. Furthmüller, Efficient iterative schemes for ab initio total-energy calculations using a plane-wave basis set. *Phys. Rev. B* **54**, 11169 (1996).
59. M. E. J. Heyd, G. E. Scuseria, Hybrid functionals based on a screened coulomb potential. *J. Chem. Phys.* **118**, 8207–8215 (2003).
60. L. G. S. Grimme, S. Ehrlich, Effect of the damping function in dispersion correcteddensity functional theory. *J. Comput. Chem.* **32**, 1456–1465 (2011).
61. H. Fang *et al*., Stabilizing $Ti_3C_2T_x$ MXene Flakes in Air by Removing Confined Water. Open Science Framework. https://doi.org/10.17605/OSF.IO/GWPDV. Deposited 14 June 2024.